Flight Data Analysis of the HyShot 2 Scramjet Flight Experiment

Michael K. Smart[*] and Neal E. Hass[†]
NASA Langley Research Center, Hampton, Virginia 23681
and
Allan Paull[‡]
University of Queensland, Brisbane 4072, Australia

The development of scramjet propulsion for alternative launch and payload delivery capabilities has been composed largely of ground experiments for the last 40 years. With the goal of validating the use of short duration ground test facilities, a ballistic reentry vehicle experiment called HyShot was devised to achieve supersonic combustion in flight above Mach 7.5. It consisted of a double wedge intake and two back-to-back constant area combustors; one supplied with hydrogen fuel at an equivalence ratio of 0.34 and the other unfueled. Of the two flights conducted, HyShot 1 failed to reach the desired altitude due to booster failure, whereas HyShot 2 successfully accomplished both the desired trajectory and satisfactory scramjet operation. Postflight data analysis of HyShot 2 confirmed the presence of supersonic combustion during the approximately 3 s test window at altitudes between 35 and 29 km. Reasonable correlation between flight and some preflight shock tunnel tests was observed.

Nomenclature

f	=	aerodynamic factor
h	=	altitude, km
k	=	5.291e-9 kg/s/Pa
M	=	Mach number
$\dot{m}_f$	=	fuel flow rate, kg/s
p	=	pressure, kPa
q	=	dynamic pressure, kPa
R	=	radius, mm
T	=	temperature, K
t	=	time, s
V	=	velocity, m/s
w	=	mass flow, kg/s
x	=	axial coordinate
y	=	lateral coordinate
Z	=	normal coordinate
α	=	angle-of-attack, deg
γ	=	ratio of specific heats
ϕ	=	equivalence ratio = fuel mass fraction/stoichiometric mass fraction
ω	=	angular velocity about longitudinal body axis, radian/s
ζ	=	angular velocity of longitudinal axis about velocity vector, radian/s

Subscripts

0	=	freestream
c	=	combustor entrance
comb	=	combustor
f	=	fuel
$t2$	=	pitot
w	=	wedge

Introduction

THE theoretical performance advantage of scramjets over rockets in hypersonic flight has been well known since the 1950s. For this reason, significant scramjet research has been conducted in many parts of the world [1]. Ground testing in continuous flow facilities has composed most of the scramjet testing below Mach 8 [2], whereas shock tunnels with flow durations of the order of 1–10 ms have been used for testing above Mach 7. The Center for Hypersonics at the University of Queensland has routinely performed scramjet testing in shock tunnels for many years [3]. Based on the desire to validate such testing for conditions in the Mach 7–8 regime, a sounding rocket based flight project known as HyShot was devised. This project involved two flight tests of a simplified supersonic combustion experiment designed solely through shock tunnel testing. Although the HyShot scramjet payload was elegantly simple and quite robust, significant issues associated with providing suitable scramjet flight test conditions with the available rocket needed to be overcome. The chosen solution to these issues resulted in a highly parabolic trajectory, with the scramjet experiment being conducted during an almost vertical reentry [4]. Following a first launch failure on 30 October 2001, the University of Queensland conducted a successful second launch on 30 July 2002. Some details of this novel approach are described here, along with a discussion of how the trajectory was reconstructed solely from onboard measurements. Flight data analysis is then presented, along with comparison to some preflight shock tunnel data.

Flight Profile Overview

Both HyShot flights took place at the Woomera Prohibited Area Test Range in central Australia. Each used a two-stage Terrier–Orion Mk70 rocket that generated a highly parabolic trajectory to boost the payload and the exhausted second stage Orion motor to an apogee in excess of 300 km, as shown in Fig. 1. This combination of rocket and trajectory allowed the payload and attached second stage motor to reenter the atmosphere with a Mach number in excess of 7.5 between 35 and 25 km altitude, thus supplying a useful range of flight conditions for the testing of a scramjet. The almost vertical initial portion of this trajectory (the launch rail being at 77 deg) lifted the payload quickly out of the atmosphere, therefore reducing both the

*Research Scientist, Hypersonic Airbreathing Propulsion Branch; presently Associate Professor, Division of Mechanical Engineering, University of Queensland.
†Aerospace Engineer, Hypersonic Airbreathing Propulsion Branch.
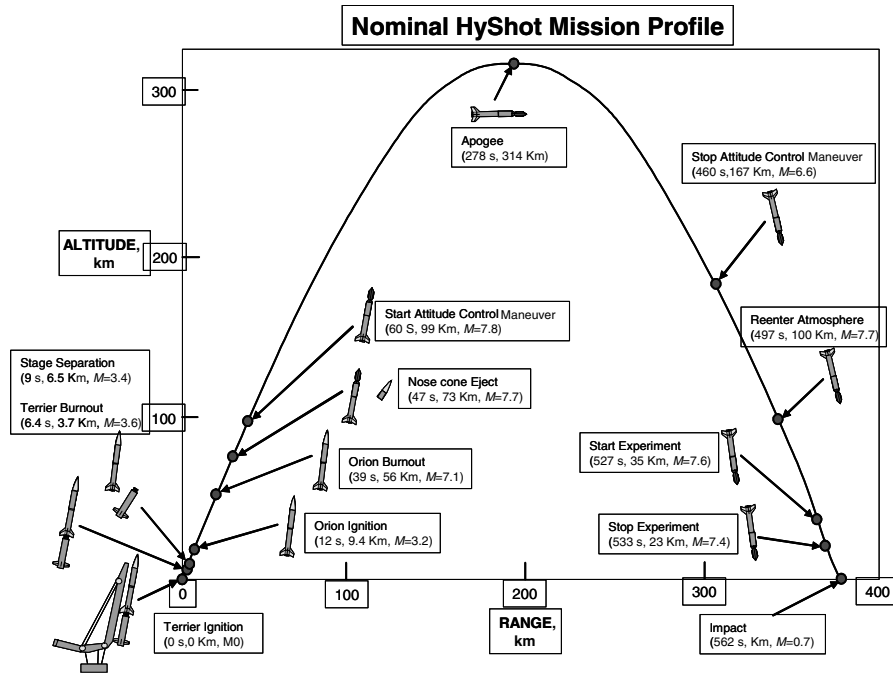‡Professor, Division of Mechanical Engineering.

Fig. 1 HyShot flight profile.

payload/rocket aerodynamic heating loads and the integrated drag. This allowed for a relatively simple payload design, and a very high test Mach number for the combination of a Terrier–Orion booster and a 110 kg payload. The main difficulty with this trajectory was the maintenance of stable flight upon reentry into the atmosphere. This was successfully achieved through a reorientation maneuver outside the atmosphere such that the payload reentered nose-first with a time varying attitude that produced payload angle-of-attack and yaw variations of approximately ±5 deg during the scramjet experiment.

Payload Geometry

A schematic of the payload assembly is shown in Fig. 2. It included a nose cone to shroud the scramjet flowpaths on the initial ascent, two scramjet combustors orientated back-to-back on a wedge forebody, plus hydrogen and nitrogen tanks, batteries, a telemetry system, flight computer, and other components. One combustor was hydrogen fueled through four laterally spaced normal injectors,

whereas the other combustor was unfueled so as to obtain baseline (tare) conditions to compare against the fueled flowpath throughout the flight. Figure 3 shows a photograph of the payload used for flight 2 (with the shroud removed). It was constructed predominantly of copper alloy for rapid dissipation of aerodynamic and combustion generated heat loads, with tungsten-zirconium-molybdinum used for the highest heat flux regions that occur at the leading edges of both combustors.

The goal of the experiment was to supply uniform flow into the two rectangular combustors at conditions ranging between Mach 7.2 and 8.0, allowing for an angle-of-attack variation of the payload between +5 and −5 deg. To meet this goal, and also to make the experiment as simple as possible, the flowpath intake was designed to allow significant flow spillage. As a further simplifying feature, the two flowpath nozzles were designed to exhaust laterally and generate very little overall thrust. These characteristics, although not applicable to a practical scramjet where mass flow capture and thrust generation are to be maximized, eliminated risk factors associated
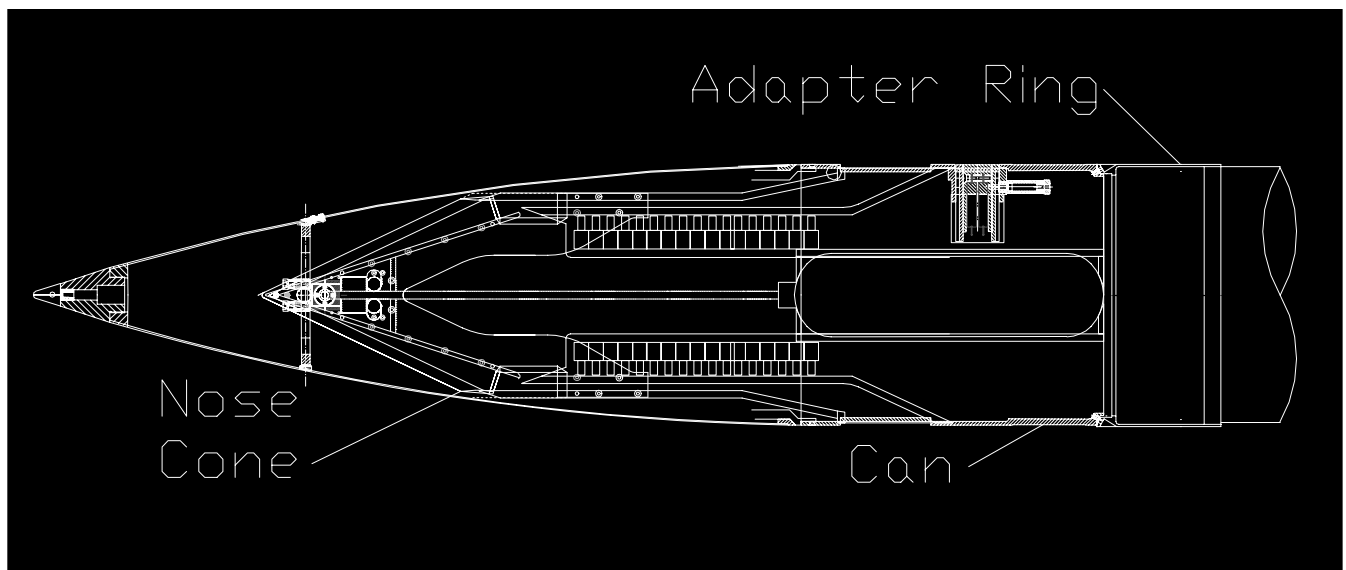

Fig. 2 Schematic of the HyShot payload.

Fig. 3 HyShot payload.

with the intake and nozzle and enabled a simplistic supersonic combustion experiment to be conducted.

Figure 4 shows a schematic of the fueled flowpath. The intake consisted of a single 18 deg wedge with a width of 100 mm, a blunted leading edge, and highly swept side fences. The high wedge angle was necessary to ensure that the combustor entrance temperature and pressure were great enough to readily induce self-ignition of hydrogen. The rectangular combustor had a constant area 9.8×75 mm cross section and a length of 300 mm (length/height = 30.61). The combustor cowl spanned the full width of the intake wedge and was situated such that the intake shock was upstream of its leading edge at all times. The flowpath design incorporated a shock trap that was situated between the end of the intake wedge and the entrance of the combustor. This feature not only captured the cowl shock, but also bled off the intake boundary layer. The reduced width of the combustor (relative to the intake wedge) and lateral spillage holes in the side fences adjacent to the shock trap

were designed to remove the fence boundary layers and corner flows. The angle-of-attack of the payload is defined as positive when the fueled combustor was on the windward side, and negative when the fueled combustor was leeward.

Instrumentation

Instrumentation carried by the payload included pressure transducers, ceramic thermisters (thermoresistors), thermocouples, accelerometers, magnetometers, and horizon sensors. The onboard battery voltage was also measured. The pressure transducers used for the flight were SenSym 19 C series and SenSym 13 mm series absolute pressure gauges covering various ranges from 0–15 psi (0–103 kPa) for thrust surface measurements, to 0–5000 psi (0–34 MPa) for the hydrogen fuel tank pressure. The error associated with the use of these transducers, in concert with the flight data acquisition system, was estimated to be ±0.5% full scale.

Fourteen pressure measurements were made along the bodyside wall of each combustor. Figure 5 displays the position of these measurements relative to the combustor entrance. The combustor entrance is defined as the axial position of the virtual leading edge of the bodyside combustor wall. Both combustor sidewalls began at this same axial position, whereas the cowl projected further forward. Thirteen of the pressure measurements were made on the centerline, beginning 103.6 mm from the combustor entrance and continuing at 22 mm intervals. An additional measurement (labeled PA14 in the fueled combustor and PB14 in the unfueled combustor) was made 25 mm away from the centerline, a distance 290.6 mm from the combustor entrance (Fig. 5). A single pressure measurement was also made on each intake wedge at a wetted distance of 59.4 mm from the virtual leading edge of the intake wedge and 3.6 mm off the centerline. Unfortunately, the intake wedge surface pressure measurement for the unfueled combustor lagged that of the fueled intake wedge, and continually degraded as dynamic pressure increased. It is postulated that there was a leak in the transducer sensing line, hence this measurement was not used in the analysis.

All pressure transducers were mounted close to the backside of each surface to provide a short response time. This was dictated by the expected 30% pressure variation every 70 ms due to a payload spin rate in excess of 5 Hz and angle-of-attack variation between +5 and −5 deg. However, the mounting point was also sufficiently far from the wall to provide for thermal protection of the transducers during the test window of the experiment. All transducers measured absolute values and were temperature compensated. The uncertainty associated with all pressure measurements is indicated at appropriate positions in the text.

One temperature measurement was made on the backside of each of the bodyside combustor walls using a thermoresistive sensor. These were located 279.6 mm from the combustor entrance and 20 mm off the centerline, on the opposite side of the centerline to the fourteenth pressure transducer, and are denoted by ETA (ETB) in Fig. 5.
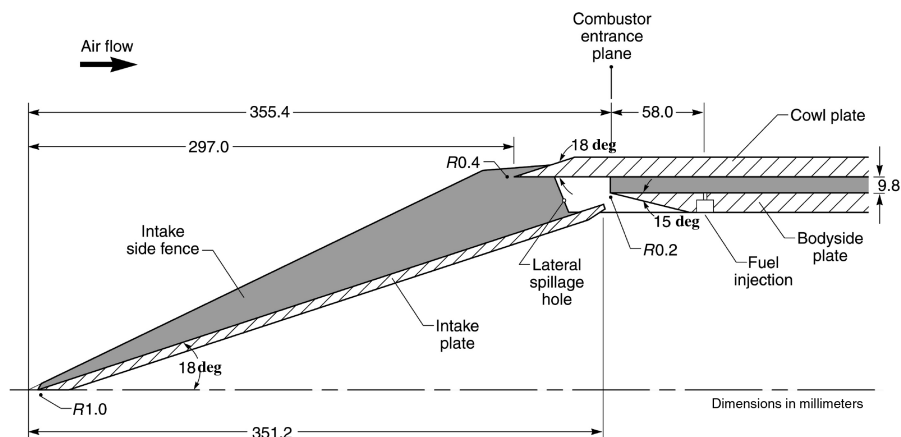

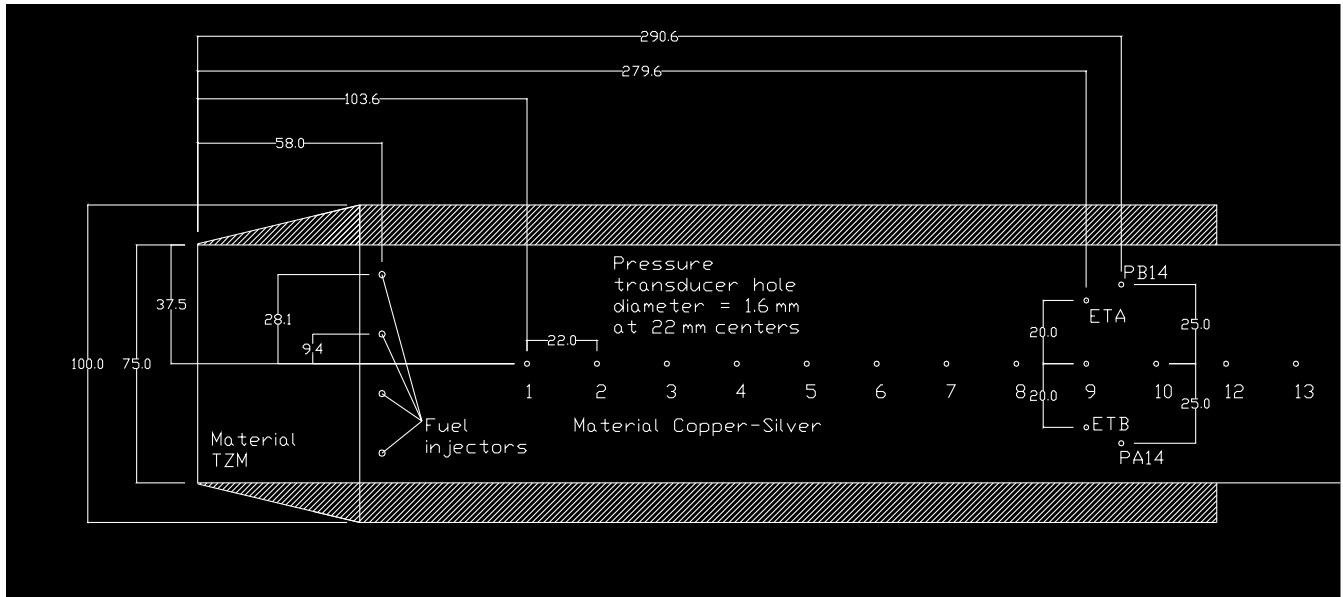Fig. 4 Schematic of fueled flowpath.

Fig. 5   Combustor instrumentation layout and injector location (all measurements in millimeters).

To determine free stream conditions during reentry, two pitot probes were mounted on either side of the intake (each with two transducers attached in parallel) as indicated in Fig. 6. These transducers had different ranges so as to cope with the variations in atmospheric pressure during reentry. The higher sensitivity gauges were appropriate for pressures up to 101 kPa. The secondary set were used from 80 kPa and above, and were linear to 350 kPa.

Four accelerometers were mounted in the payload. Two measured the acceleration in the nominal direction of motion (x axis) with different ranges and sensitivities. The other two measured the accelerations in two planes perpendicular to the nominal direction of motion (y and z axes). The magnetometer and horizon sensor were utilized during the exoatmospheric reorientation maneuver.

All data were sampled approximately every 2 ms, and a total of 48 analog and 4 digital channels were broadcast and recorded on the ground. There are no tracking data of the experiment trajectory due to a loss of radar lock immediately after the launch.

Fuel Supply System

The fuel used in the experiment was gaseous hydrogen. It was contained in a 3 liter tank with a maximum supply pressure of 21 MPa. The fueled flowpath was fed by four 2.0-mm-diam normal sonic injection ports 58 mm downstream of the combustor entrance on the bodyside (see Fig. 5). The pressure transducer used to control and monitor the fuel flow rate was mounted between the fuel control valve and the injectors. The fuel system was calibrated on the ground

to determine a calibration constant between the measured fuel line pressure and the fuel mass flow rate. This relationship is given by

$$\dot{m}_f = k p_f \qquad (1)$$

Fuel flow was triggered by and metered relative to the measured pitot pressure. Preflight ground tests [5] had indicated that equivalence ratios greater than 0.5 could separate the boundary layer in the constant area combustor. For this reason, the metering valve was preset to maintain a fuel equivalence ratio of approximately 0.3 throughout the majority of the expected test window. Near the end of the experiment, the fueling was scheduled to increase in an attempt to unstart the fueled combustor.

Flight Test

The atmospheric conditions at Woomera for the 30 July 2002 launch were near optimal. Launch site atmospheric pressure was just over 1000 mbar and there was no significant cloud cover. Balloon measurements indicated favorable conditions throughout the launch trajectory with atmospheric properties that very nearly matched 1976 standard atmospheric conditions. Ground temperatures at launch were near 15°C with surface winds well below restriction limits. The launch proceeded with the test article clearing the rails without event. Shortly thereafter, the launch site radar tracking station lost its lock on the telemetry and the vehicle. The downrange radar tracking station picked up telemetry radiation shortly after launch, however, the vehicle was never reacquired by either radar station. Fortunately, telemetry coverage from both sources overlapped and telemetry for the whole trajectory was captured. Unfortunately, there was no radar tracking data to determine vehicle velocity and position.

Trajectory Reconstruction

Because of the failure of radar tracking, the HyShot 2 trajectory was reconstructed from onboard accelerometer, pressure transducer, magnetometer, and horizon sensor measurements. The most detailed reconstruction to date is described in [6], and is the source for all trajectory information used in this paper.

The HyShot 2 flight trajectory may be broken into three phases: launch, space, and reentry. The launch phase involved the first stage Terrier burn, separation of the used Terrier motor, a second stage Orion burn, and blowoff of the nose cone. This phase of the trajectory was reconstructed by integration of the axial accelerometer measurements, utilizing the assumption that the vehicle axis was aligned with the flight path. Based on this analysis, at $t = 60.5$ s after
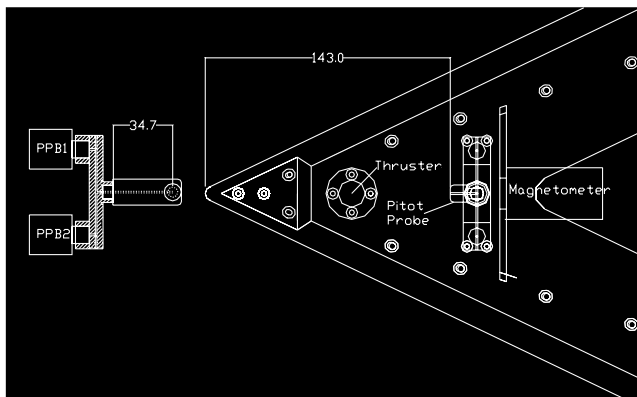

Fig. 6   Payload leading edge showing pitot probe and magnetometer location (all measurements in millimeters).
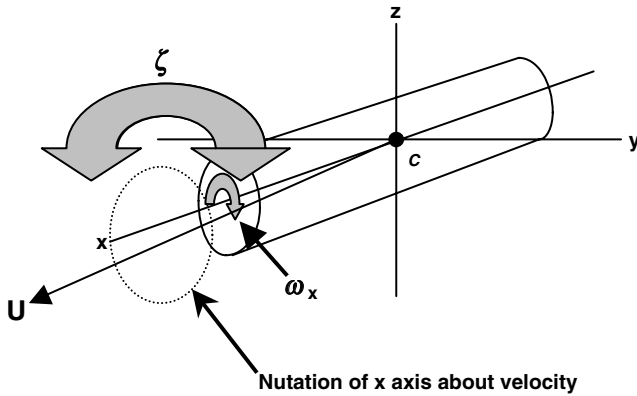
Fig. 7 Schematic of a rolling and nutating body

launch the payload/Orion motor (denoted as the "vehicle") was at an altitude of 99.25 km, a velocity of 2185.6 m/s, and a flight path angle of 69.7 deg. During the space phase of the trajectory, the vehicle reached an apogee of 328.27 km and conducted a reorientation maneuver to produce a nose-down reentry. The velocity, altitude, and flight path angle for this phase of the trajectory were reconstructed using conservation of energy and momentum methods, and the change in vehicle attitude caused by the reorientation was determined through magnetometer and horizon sensor measurements. Based on these analyses, the vehicle ended the space phase of the trajectory at $t = 512.8$ s at an altitude of 99.25 km, with a velocity of 2185.6 m/s, and a flight path angle of -69.6 deg. The vehicle attitude at this stage of the trajectory varied with time as a result of a combination of roll and nutation. Roll is a rotation of the vehicle about its axis and nutation is a coning of the body axis about the velocity vector, as is shown in Fig. 7. Based on the magnetometer and horizon sensor measurements, at the end of the space phase the vehicle was rolling at 5.2 Hz and nutating at an angle of 39 deg relative to the flight path. The angle-of-attack and yaw of the reentering vehicle therefore undulated in a cyclic manner with amplitudes that varied with time.

The reentry phase of the trajectory was reconstructed from integration of the axial accelerometer measurements, however, this task was complicated by the fact that the vehicle axis was not aligned with the flowpath angle, and that the vehicle state at the end of the space phase was not known with sufficient accuracy to be used as an initial condition for reentry integration (due to inadequate accuracy of the acceleration measurements [6]). The effect of the vehicle attitude was accounted for by multiplying the axial acceleration measurements by a factor

$$f = 1 + 0.1\alpha + 11.9\alpha^2 \qquad (2)$$

determined from aerodynamic testing of the vehicle described in [7]. The time history of α needed to calculate f was determined from
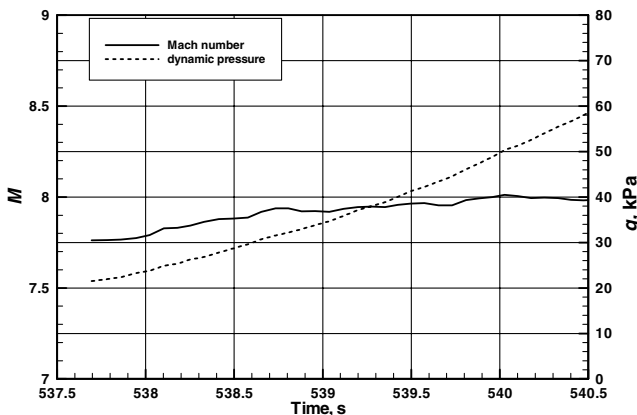
pressure measurements, as described later. An accurate estimate of the vehicle state at the start of the reentry phase was determined by comparison with the measured pitot pressure time histories. As described in [6], this process involved multiple trajectory integrations starting with a matrix of initial values for velocity and altitude (and the use of the 1976 standard atmospheric tables), to determine the combination that most closely matched the measured pitot pressure history. This analysis [including the use of Eq. (2) for f] resulted in an initial state for the reentry phase of the trajectory at an altitude of 99.25 km, as $t = 508$ s with a velocity of 2172.9 m/s, and a flight path angle of -69.2 deg. No error estimation for these conditions has been made to date.

The goal of the flight was to fly a reentry trajectory that supplied a multisecond window of flight at conditions appropriate for scramjet operation slightly above Mach 7.5. Figure 8 shows the time histories of Mach number and dynamic pressure calculated using the reconstructed reentry trajectory covering the period when the scramjet experiment took place. During this 3 s window, starting at $t = 537.5$ s, the Mach number remained between $M_0 = 7.75$ and 8.0, which is slightly higher than the maximum value of 7.6 anticipated from preflight modeling of the trajectory. The observed jagged appearance of the Mach number time history during the experimental window is believed to be due to lack of conditioning of the accelerometer measurements. Figure 8 also shows that the dynamic pressure increased rapidly from $q_0 = 21.0$ to 58.5 kPa throughout the 3 s time window as the vehicle descended from an altitude of 34.9 to 28.1 km.

Flight Data Analysis

Analysis of the flight data began with the two measured pitot pressure histories, which had an uncertainty of ± 0.5 kPa, and are plotted in Fig. 9a over a 1 s interval during the 3 s test window. The first thing to note about these measurements is that although both

a) Pitot probe histories
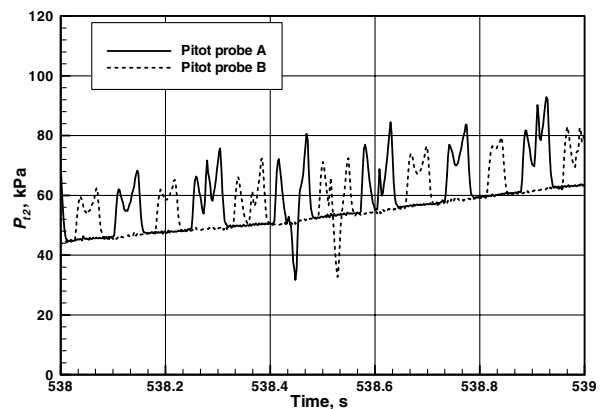
Fig. 8 Reconstructed Mach number and dynamic pressure histories.
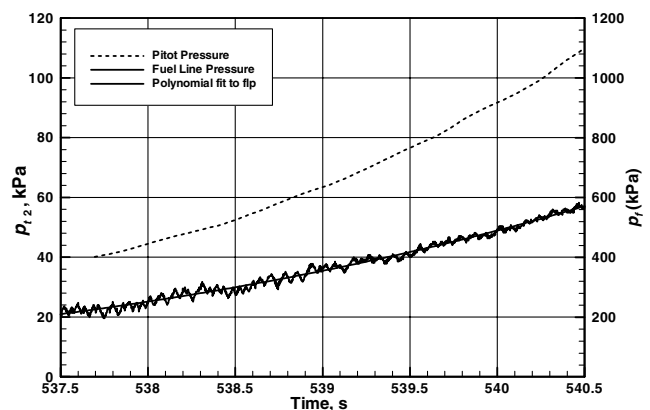
b) Pressures used for analysis

Fig. 9 Pitot pressure and fuel line pressure histories.

pitot pressures increased smoothly for portions of the time window, for other portions the pitot pressures took periodic excursions to much higher levels. Also note that the excursions of the probes are out of phase with each other. Recalling that probes A and B are offset from opposite sides of the payload (Fig. 6), it is clear that this behavior was due to the roll and nutation of the vehicle, causing each probe to pass periodically behind the vehicle bow shock. The pitot pressure time history that is applicable for flight data analysis is therefore represented by the smooth line shown in Fig. 9b, which is an average of both probe measurements with the excursions removed and plotted over the full 3 s experimental window. Also shown in Fig. 9b is the fuel line pressure history for the fueled combustor, which was proportional to the fuel flow rate history [see Eq. (1)], and had an uncertainty of ±6.9 kPa. As already discussed, hydrogen flow to the fuel injectors was designed to be initiated when the measured pitot pressure crossed a preflight determined threshold. The flight data indicated that this did in fact occur, with fuel flow commencing at $t = 536.47$ s at a pitot pressure level of approximately $P_{t2} = 34$ kPa.

The time history of the fueled intake wedge pressure measurement, which had an uncertainty of ±0.5 kPa, is shown in Fig. 10. The undulations caused by the roll and nutation of the vehicle are evident in the figure. Examination of the time between peaks results in an estimate of the roll frequency during the experiment window of $1/0.16 = 6.25$ Hz. Examination of a full nutation cycle results in an estimate of the nutation frequency during the experimental time window of $1/0.63 = 1.6$ Hz. Based on the geometry of the payload and these roll and nutation frequencies, the maximum rotational velocity of the payload was approximately 3 m/s, i.e., almost 3 orders of magnitude smaller than the total velocity of the vehicle, and was therefore inconsequential to the experiment.

As the vehicle rolled and nutated, its attitude cycled from time slices with the payload at zero yaw and the fueled side at positive α, through times with zero α and high yaw, to times with zero yaw and the fueled side at negative α. The time slices when the intake pressures were at maximum or at minimum corresponded to when the intake wedges were at zero yaw. The time slices obtained when the intake pressure for the fueled combustor was at maximum corresponded to the maximum positive α for that cycle. These are referred to as windward time slices for the fueled combustor. Because of the back-to-back configuration of the two combustors, these time slices also corresponded to the minimum pressure on the intake of the unfueled combustor, which are referred to as leeward time slices for the unfueled combustor. In a similar manner, time slices obtained when the intake pressure for the fueled combustor was at minimum corresponded to the maximum negative α, and are referred to as leeward conditions for the fueled combustor and windward conditions for the unfueled combustor. Only data at time slices corresponding to zero yaw are examined here.

Vehicle angle-of-attack was determined using the Rankine–Hugoniot relations, which for a calorically perfect gas supply the following formula for the ratio of the intake wedge pressure and the pitot pressure

$$\frac{p_w}{p_{t2}}$$
$$= \left\{ \frac{2\left[2\gamma M_0^2\sin^2(18+\alpha)-(\gamma-1)\right]\left[(\gamma-1)M_0^2\sin^2(18+\alpha)+2\right]}{(\gamma+1)^2 M_0^2\sin^2(18+\alpha)[(\gamma-1)M_0^2+2]} \right\}^{\frac{\gamma}{\gamma-1}}$$

(3)

The unknowns in Eq. (3) are α, γ, and M_0. However, this relation is insensitive to Mach number variations between $M_0 = 7.5$ and 8.0 (the range of interest in the time window of the experiment), and variations in γ due to thermal effects, therefore, the time history of α was determined by using values of $M_0 = 7.75$ and $\gamma = 1.40$ in Eq. (3), and substitution of the measured time histories of the fueled intake wedge pressure and the pitot pressure. Figure 11 shows the calculated α during the test window, clearly indicating the effects of both roll and nutation on the angle-of-attack experienced by the vehicle.

Figures 8 and 11 were used to determine the most appropriate zero yaw time slices for combustor data analysis. The criteria used for this were 1) $q_0 > 23.94$ kPa (500 psf), 2) $\alpha < 6$ deg, and 3) as early as possible during the experimental window. Table 1 shows the flight parameters of the four time slices examined in this article. These are all at relatively constant Mach number but increasing dynamic pressure. Time slices 1 and 3 correspond to windward conditions for the unfueled combustor (leeward for the fueled combustor), whereas time slices 2 and 4 correspond to leeward conditions for the unfueled combustor (windward for the fueled combustor).

Combustor Entrance Conditions

The geometry of the scramjet payload, its flight profile, and its attitude were all devised to produce uniform combustor entrance conditions suitable for a supersonic combustion experiment. It was intended to calculate these combustor entrance conditions by simply processing the freestream flow with two oblique shocks. However, it became clear that both leading edge bluntness effects and laminar boundary layer growth on the intake and cowl could not be neglected. The combustor entrance conditions were therefore calculated using NASA Langley's VULCAN code, which is a general purpose CFD code that solves the Reynolds averaged Navier–Stokes equations [8]. A two-dimensional (2-D) grid with almost 85,000 cells was used to model the flow in the intake and combustor of the scramjet payload in this instance, with no fuel injection. Inviscid fluxes were modeled using Edwards' low-dissipation flux-split scheme [9], with second-order MUSCL interpolation, and Van Leer's flux-limiter. Based on the natural boundary layer transition criteria of $Re_\theta/M = 285$ (see [10]), the flow was assumed to be laminar up to a short distance
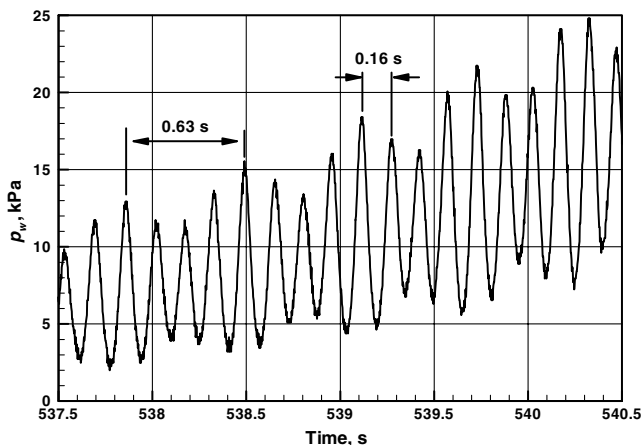

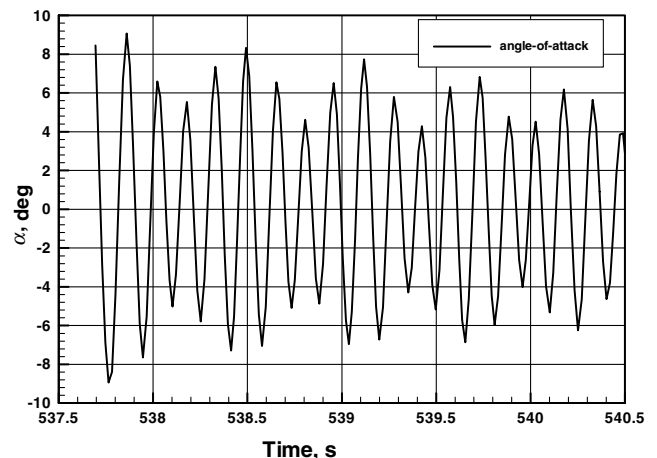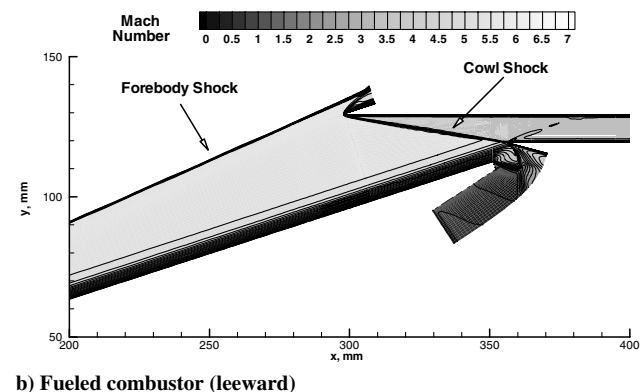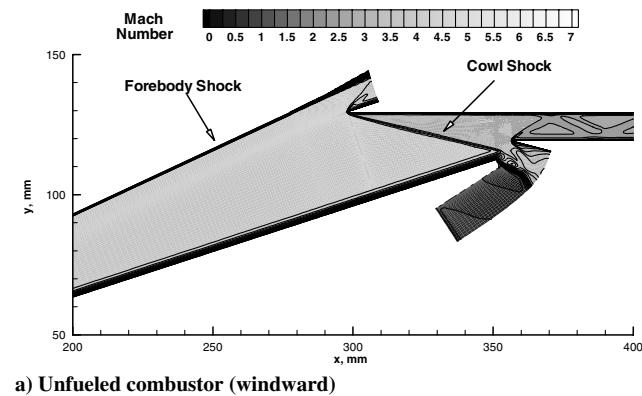Fig. 10   Intake wedge pressure history for the fueled combustor.

Fig. 11   Vehicle angle-of-attack history.

Table 1 Flight parameters for analyzed time slices

Number	Time, s	M_0	q_0 (kPa)	h (km)	α (deg)
1	538.103	7.828	24.88	34.48	−5.012
2	538.179	7.831	25.33	34.31	5.540
3	538.734	7.938	31.55	33.05	−5.081
4	538.805	7.938	32.20	32.89	4.617

Table 2 Entrance conditions for the unfueled combustor

Number	Time, s	p_c (kPa)	T_c (K)	M_c	w (kg/s)
1	538.103	43.446	1395.9	2.430	0.1405
2	538.179	26.047	989.52	3.273	0.1361
3	538.734	55.256	1388.4	2.436	0.1797
4	538.805	35.889	1006.9	3.224	0.1829

Table 3 Entrance conditions for the fueled combustor

Number	Time, s	p_c (kPa)	T_c (K)	M_c	w (kg/s)	ϕ
1	538.103	26.789	1004.5	3.237	0.1372	0.345
2	538.179	44.847	1416.6	2.393	0.1418	0.346
3	538.734	33.778	991.8	3.262	0.1754	0.335
4	538.805	55.640	1370.1	2.470	0.1848	0.327

upstream of the injectors, and Menter's k–ω model [11] was used for the remainder of the domain. The turbulent Prandtl number was set at 0.9 and Wilcox's wall-matching functions and compressibility correction [12] were used. The thermodynamic model used was a single-species model for air available with VULCAN distribution. The grid convergence or discretization error of the CFD solutions was determined by comparing combustor entrance conditions calculated on the ∼85, 000 cell "fine" grid with those calculated on a "coarse" grid with double the grid spacing. The relative difference $\varepsilon = (g_c - g_f)/g_f$ of these solutions, where g_c and g_f represent typical combustor entrance properties on the coarse and fine grids, respectively, was less than 1.1%.

Figure 12a shows the Mach number distribution of the flow entering the unfueled combustor calculated with VULCAN at time slice 1. The forebody and cowl shocks are labeled in the figure, with the shock trap performing its desired function for this windward condition. The laminar boundary layer on the forebody wedge is clearly visible and flow entering the combustor is relatively uniform. The Mach number contours reflecting across the combustor are due to the shock from the blunt leading edge on the bodyside of the combustor entrance, which persists well into the combustor. Figure 12b shows the calculated Mach number distribution of the flow entering the fueled combustor at time slice 1. For this leeward condition, the cowl shock strikes the bodyside combustor leading edge head-on, indicating that the shock trap performance is marginal at these conditions. The forebody boundary layer is also thicker than for the windward case, and has a small effect on the combustor entrance conditions.

The flow features shown in Figs. 12a and 12b are typical of all time slices. The flux conserved combustor entrance conditions calculated using VULCAN for the unfueled combustor at all four time slices are shown in Table 2. Table 3 lists the flux conserved combustor entrance conditions for the fueled combustor, along with the equivalence ratio corresponding to the fuel flow rate measured at each time. As already noted, the fuel flow rate was metered relative to the measured pitot pressure, and did not account for the effect of angle-of-attack on the fueled combustor mass capture. Despite this, equivalence ratio values at each of the time slices of interest varied by 6% and averaged $\phi = 0.338$, slightly above the goal of $\phi = 0.3$.

Combustor Data Analysis

Analysis of the combustor flight data began with a comparison of the unfueled combustor with the 2-D CFD calculations. The uncertainty associated with these measurements was ±1.7 kPa. Figure 13 shows a typical result, in this instance a windward case at time slice 3. The first thing to note is that the CFD gives a clear indication of the effect of the shock from the blunt leading edge ($R = 0.2$ mm) of the bodyside combustor wall. This shock, which is due solely to the small leading-edge bluntness, crosses the duct numerous times along its length, generating pressure fluctuations as high as 35% of the combustor entrance pressure. This effect is somewhat masked in the flight data which, due to its sparse nature, gives a misleading view of the shape of the pressure distribution in this shock dominated flow. In addition to the shock interactions, both the flight data and the CFD show a gradual pressure rise along the duct due to boundary layer growth. It is also clear in Fig. 13 that the 2-D CFD underpredicts the overall level of the flight pressure data along the combustor by approximately 10%. Underprediction of this magnitude was not unexpected, as three-dimensional effects such as boundary layer growth along the combustor sidewalls (length/width = 4) and pressure variations due to shocks from the

a) Unfueled combustor (windward)

b) Fueled combustor (leeward)

Fig. 12 CFD generated Mach number distributions in the intake at Time Slice 1.
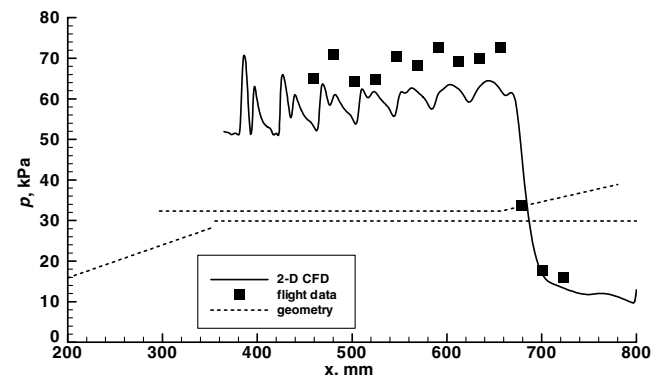
Fig. 13 Comparison between 2-D CFD and flight data for the unfueled combustor at windward conditions.
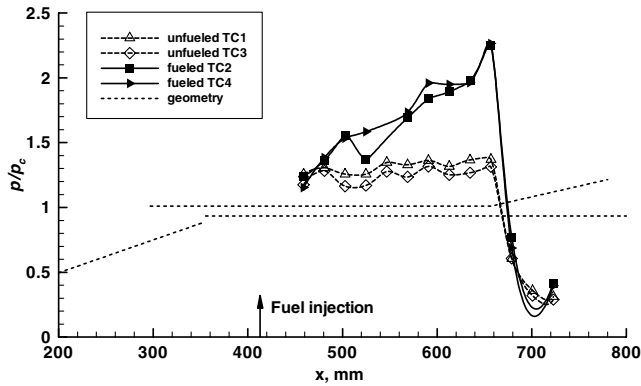
Fig. 14   Windward fueled and unfueled combustor pressure distributions.

combustor side leading edges ($R = 0.2$ mm) would act to increase combustor pressure.

The key aspect of the flight experiment was the generation of supersonic combustion, the extent of which can be best gauged by comparison between fueled and unfueled combustor data. As already noted, the uncertainty associated with measurements in the unfueled combustor was ± 1.7 kPa, whereas the uncertainty of measurement in the fueled combustor was ± 3.4 kPa. Figure 14 shows a comparison of the fueled and unfueled combustor pressure data for windward conditions when all data is normalized by the corresponding combustor entrance pressure (Tables 2 and 3), to remove differences associated with variations in dynamic pressure and angle-of-attack. Both fueled and unfueled data show a similar pressure level at the first tap (45.6 mm downstream of fuel injection), indicating little or no combustion up to this point. By the third pressure tap (99.6 mm downstream of fuel injection), however, the fueled combustor data had a significantly higher normalized pressure than the unfueled data. This pressure rise, due to the combustion of hydrogen, increased down the duct and was only truncated by the expansion fan from the shoulder of the nozzle. The normalized peak pressure at the end of the fueled combustor was a factor of 2.26 times the combustor entrance pressure. Assuming this is representative of combustion generated pressure rise in the duct, one-dimensional equilibrium cycle analysis was performed to determine what level of hydrogen combustion would be consistent with this pressure rise. Assuming an average skin friction coefficient for the duct of 0.002 and a wall temperature of 350 K (based on thermoresistor sensor data), these calculations indicated that an equivalence ratio of $\phi = 0.280$ of hydrogen was consumed. Consequently, it is estimated that supersonic combustion occurred in the fueled combustor at the windward time slices with a combustion efficiency of 81%.

Figure 15 shows a comparison of fueled and unfueled combustor pressure distributions for leeward conditions. In this instance, the pressure rise due to combustion appears to be delayed (relative to
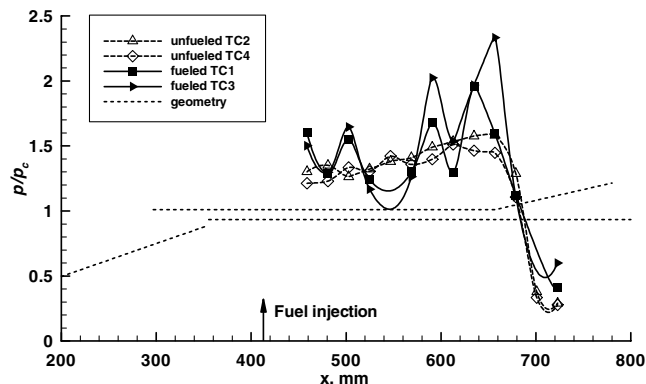
windward conditions), however, by the end of the duct the pressure in the fueled combustor was considerably higher than the unfueled combustor. Fueled combustor entrance pressures for the two leeward times slices were less than 34 kPa, and the combustor entrance temperatures were approximately 1000 k. These conditions are on the lower limit for autoignition of hydrogen, so it is not surprising that combustion was less intense than at windward conditions, where the combustor entrance pressure and temperature were approximately 50 kPa and 1400 K, respectively.

The flight data time slices used for analysis in this paper were at flight times before $t = 539$ s. This constraint on the flight data analysis was dictated by a significant change in the character of the combustor data that was observed to occur at approximately $t = 539.5$ s. Figures 16a and 16b illustrate this change quite clearly for the unfueled combustor for both windward and leeward conditions, respectively. Figure 16a shows normalized combustor pressure distributions for windward conditions at a series of zero yaw time slices between $t = 538$ and 541.5 s. Up to the $t = 539.352$ s time slice, the normalized unfueled combustor pressure distributions lay on top of each other, whereas at time slices after $t = 540.5$ s, the normalized unfueled combustor pressure distributions changed to a considerably higher pressure. The timing of this change in the character of the flight data is further substantiated by similar plots of the unfueled combustor pressure distributions at leeward conditions shown in Fig. 16b. These exhibited an increase in the combustor pressure level after the time slice at $t = 539.276$ s. Based on these observations, it is postulated that at some time close to $t = 539.5$ s the unfueled combustor underwent a geometrical change that generated significantly stronger shock waves in the combustor. This could be caused by failure and/or distortion of either the cowl or combustor leading edges, or their structural support. A similar phenomenon occurred in the fueled combustor at a slightly later time. This postulated failure precludes the analysis of time slices that occurred after $t = 539.5$ s. Fortunately, however, a significant amount of useful data was collected during the flight before this time.

a) Windward

Fig. 15   Leeward fueled and unfueled combustor pressure distributions.
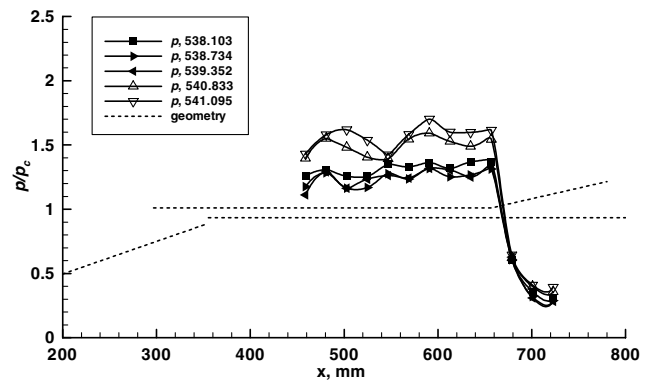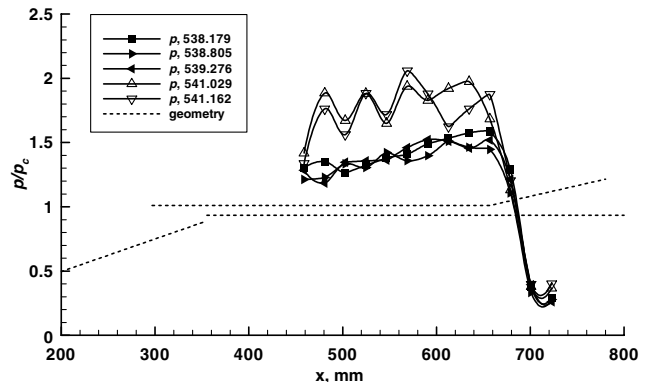
b) Leeward

Fig. 16   Unfueled combustor geometry divergence assessment.

Flight-to-Ground Comparison

One of the important motivations for the HyShot flights was validation of short duration ground testing for scramjet development. As a first step toward this, a series of preflight experiments were conducted at the University of Queensland in the T4 shock tunnel to determine the expected performance of the flight payload. These experiments were documented in [5], and four of these shock tunnel runs are compared here with the presented flight time slices.

The model used for the preflight ground tests was designed to generate similar combustor entrance conditions to flight at Mach 7.6, while using an existing Mach 6.5 shock tunnel nozzle. This dictated the use of an experimental model with a 17 deg wedge intake (compared with 18 deg in the flight payload) and shock tunnel nozzle exit conditions with higher freestream pressure and temperature than flight. The 300 mm length combustor and fuel injectors were identical to flight, except that fuel injection took place 40 mm downstream of the combustor entrance (compared with 58 mm in flight), and the ground test model had an increased number of combustor pressure taps. A final difference between the ground and flight hardware was that the nozzle expansion was situated on the bodyside of the combustor in the ground test model (compared with the cowlside for the flight hardware).

Table 4 lists the shock tunnel generated conditions and model orientation used for comparison with flight, taken from [5]. These shock tunnel runs corresponded to zero yaw flight data from the fueled and unfueled combustors at windward and leeward conditions. Table 5 lists the corresponding combustor entrance conditions and fueling levels for these ground tests. These combustor entrance conditions are quite close to those calculated for the flight times slices (Tables 2 and 3), whereas the equivalence ratio of the fueled ground tests (6863 and 6847) were slightly higher than flight. As described in [13], the typical uncertainty associated with pressure measurements in the shock tunnel is $\pm 4\%$ full scale.

Figure 17 shows the fueled and unfueled combustor pressure data collected in the T4 shock tunnel for windward conditions. Once again, all data is normalized by the corresponding combustor entrance pressure (Table 5), but the horizontal axis is now distance along the combustor (x_{comb}). Both fueled and unfueled data show a similar pressure level until 150 mm along the combustor, at which point the pressure rise due to hydrogen combustion is clearly evident, reaching a normalized value of 1.91 at the last pressure tap. Figure 18 shows the fueled and unfueled combustor pressure data collected in the T4 shock tunnel for leeward conditions. In this instance, the fueled data have a higher level than the unfueled data along most of the duct, but the overall pressure rise due to combustion is not as high as for windward conditions. As was evident in the flight data, the lower pressure and temperature at leeward conditions generated less robust combustion than windward conditions.

Figure 19 shows a comparison between ground and flight data for the fueled combustor at windward conditions. As already noted, both ground and flight data showed a clear pressure rise due to supersonic combustion of hydrogen, and Fig. 19 confirms that both ground and
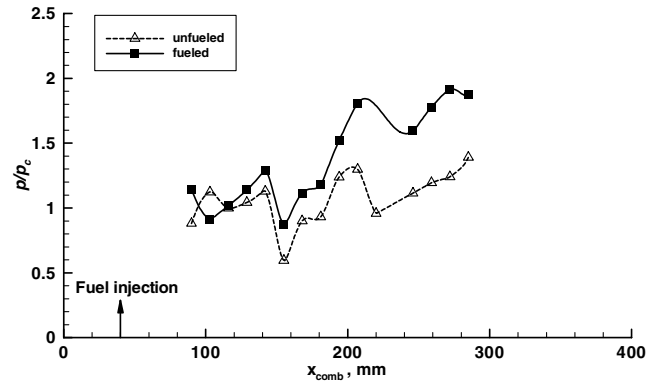

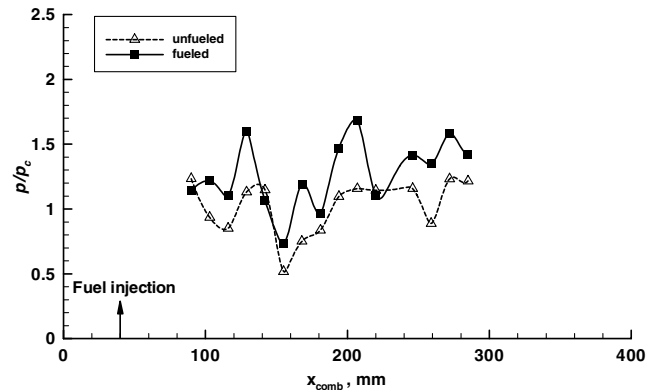Fig. 17 Ground test data at windward conditions.

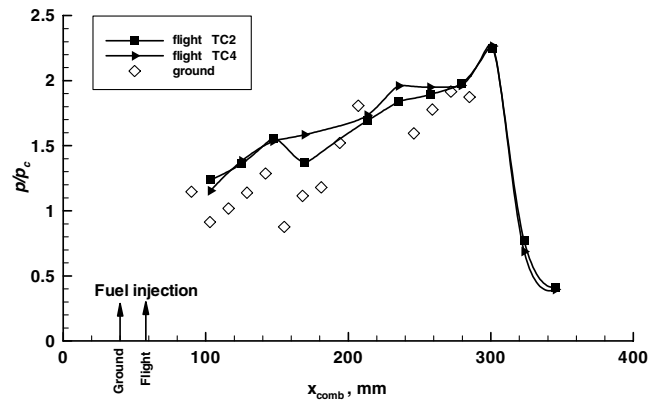
Fig. 18 Ground test data at leeward conditions.

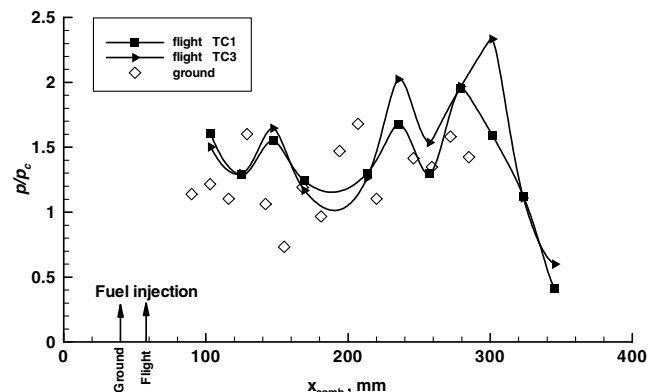Fig. 19 Flight-to-ground comparison at windward conditions.

Fig. 20 Flight-to-ground comparison at leeward conditions.

Table 4 Ground test nozzle exit conditions and model attitude

Run number	M_0	p_0 (kPa)	T_0 (K)	q_0 (kPa)	α (deg)
6844	6.500	1.043	319	30.847	4.0
6847	6.464	1.167	333	34.133	4.0
6849	6.476	1.102	328	32.351	−4.0
6863	6.484	1.022	325	30.077	−4.0

Table 5 Ground test combustor entrance conditions and fueling

Run number	M_C	p_c (kPa)	T_c (K)	ϕ
6844	2.424	42.361	1385.9	0.0
6847	2.416	46.880	1437.6	0.413
6849	3.015	29.916	1076.1	0.0
6863	3.055	27.782	1066.9	0.466

flight had similar pressure distributions along the combustor. It is interesting to note, however, that despite the fact that the ground data had a higher equivalence ratio than flight ($\phi = 0.466$ compared with $\phi = 0.346$ and 0.327), both ground and flight generated very similar normalized pressure levels at the last pressure tap in the ground model.

Figure 20 shows a comparison between ground and flight data for the fueled combustor at leeward conditions. In this instance, the fueled ground data showed less pressure rise than flight, particularly towards the end of the combustor. This may be due to the higher angle-of-attack of the flight data ($\alpha = -5.1$ deg for flight compared with $\alpha = -4.0$ deg for ground), which was on the operational limit of the shock trap (see Fig. 12b). Furthermore, interpretation of these comparisons is hampered by the different axial positions of the pressure taps in the ground and flight models. More extensive comparisons should be made when postflight ground test data become available, preferably with a model identical to the flight hardware.

Conclusions

A simple, but elegant, flight test experiment called HyShot was designed and flown above Mach 7.5 to validate the use of short duration ground test facilities for scramjet development. The scramjet payload was launched by an unguided sounding rocket on a highly parabolic trajectory to an altitude in excess 328 km. The scramjet experiment was conducted during reentry, and consisted of a double wedge intake with two back-to-back constant area combustion chambers, one fueled with hydrogen at an equivalence ratio of 0.34, and the other unfueled. Trajectory analysis, reconstructed solely from onboard measurements, indicated that the scramjet payload underwent a combination of roll and nutation during reentry that generated payload attitudes varying between ± 5 deg angle-of-attack and yaw during the scramjet experiment.

Flight data analysis was conducted at time slices when the payload was at zero yaw conditions. The useful experimental time window lasted approximately 3 s, commencing 537.5 s after launch when the payload was slightly above 35 km altitude. The data indicated that hydrogen combustion generated a pressure ratio of approximately 2.26 for windward conditions (Mach number ~ 2.4, temperature ~ 1390 K, and pressure >43 kPa at the combustor entrance). Cycle analysis indicated that this pressure rise corresponded to supersonic combustion of hydrogen at an equivalence ratio of 0.28, indicating a combustion efficiency of 81% for the scramjet. For leeward conditions (Mach number ~ 3.2, temperature ~ 1000 K, and pressure <36 kPa at the combustor entrance), there was a noticeable delay in the onset of combustion, relative to windward conditions, and lower overall pressure rise. Based on these results, it appeared that the higher Mach number and lower temperature and pressure of the leeward conditions led to less efficient combustion than occurred at windward conditions.

At approximately 540 s after launch, the pressure distributions in both the fueled and unfueled combustors deviated from expected levels. This is believed to be due to the onset of mechanical failure of some portion of the payload, therefore precluding data analysis beyond this point in the flight trajectory. Comparison between flight and short duration ground tests conducted before the flight with a model similar to the flight payload demonstrated reasonable correlation at windward conditions, but the comparison at leeward conditions was more difficult to interpret. Further ground testing is needed with a model identical to flight to fully quantify any differences between flight and shock tunnel ground data.

References

[1] Curran, E. T.,"Scramjet Engines: The First Forty Years," *Journal of Propulsion and Power*, Vol. 17, No. 6, 2001, pp. 1138–1148.

[2] Guy, R. W., Rogers, R. C., Puster, R. L., Rock, K. E., and Diskin, G. S., "The NASA Langley Scramjet Test Complex," AIAA Paper 96-3243, 1996.

[3] Paull, A., Stalker, R. J., and Mee, D. J., "Experiments on Supersonic Combustion Ramjet Propulsion in a Shock Tunnel," *Journal of Fluid Mechanics*, Vol. 296, 1995, pp. 159–183.

[4] Paull, A., Alesi, H., and Anderson, S., "HyShot Flight Program and how it was Developed," AIAA Paper 02-4939, Sept. 2002.

[5] Paull, A., Frost, M., and Alesi, H., "HyShot-T4 Supersonic Combustion Experiments," Univ. of Queensland, Rept. NAG-1-2113, Brisbane, Australia, 2000.

[6] Cain, T., Owens, R., and Walton, C., "Reconstruction of the HyShot 2 Flight from Onboard Sensors" *Proceedings of the Fifth European Symposium on Aerothermodynamics for Space Vehicles*, edited by S. Danesy, ESA Publications, Noordwijk, The Netherlands, 2005.

[7] Owens, R., and Cain, T., "HyShot 2 Aerodynamics," *Proceedings of the Fifth European Symposium on Aerothermodynamics for Space Vehicles*, edited by S. Danesy, ESA Publications, Noordwijk, The Netherlands, 2004.

[8] White, J. A., and Morrison, J. H., "A Pseudo-Temporal Multi-Grid Relaxation Scheme for Solving the Parabolized Navier–Stokes Equations," AIAA Paper 99-3360, Jan. 1999.

[9] Edwards, J. R., "A Low-Diffusion Flux-Splitting Scheme for Navier–Stokes Calculations," *Computers and Fluids*, Vol. 26, No. 6, 1997, pp. 635–659.

[10] Thompson, R. A., Hamilton, H. H., Berry, S. A., Horvath, T. J., and Nowak, R. J., "Hypersonic Boundary Layer Transition for X-33 Phase 2 Vehicle," AIAA Paper 98-0867, 1998.

[11] Menter, F. R., "Improved Two-Equation k–ω Turbulence Models for Aerodynamic Flows," NASA TM 103975, Oct. 1992.

[12] Wilcox, D. C., *Turbulence Modeling for CFD*, 2nd ed., DCW Industries, La Canada, CA, 1998.

[13] Goyne, C. P., "Skin Friction Measurements in High Enthalpy Flows at High Mach Numbers," Mechanical Engineering Ph.D. Thesis, Univ. of Queensland, Brisbane, Australia, 1998.

K. Kailasanath
Associate Editor